Rainfall erosivity in catchments contaminated with fallout from the Fukushima Dai-ichi nuclear power plant accident

J.P. Laceby[1], C. Chartin[2], O.Evrard[1], Y.Onda[3], L. Garcia-Sanchez[4], O. Cerdan[5]

[1]Laboratoire des Sciences du Climat et de l'Environnement (LSCE), Unité Mixte de Recherche 8212 (CEA-CNRS-UVSQ/IPSL), Université Paris-Saclay, Gif-sur-Yvette, France
[2] Georges Lemaître Centre for Earth and Climate Research, Earth and Life Institute, Université catholique de Louvain, Belgium
[3]Graduate School of Life and Environmental Sciences, Center for Research in Isotopes and Environmental Dynamics (CRIED), University of Tsukuba, Tsukuba, Japan
[4]Laboratoire de Biogéochimie, Biodisponibilité et Transferts de Radionucléides, IRSN/PRP-ENV/SERIS/L2BT, Cadarache, France
[5] Bureau de Recherches Géologiques et Minières, Orléans, France

Correspondence to: J.P. Laceby (placeby@lsce.ipsl.fr)

Abstract:

The Fukushima Dai-ichi nuclear power plant (FDNPP) accident in March 2011 resulted in the fallout of significant quantities of radiocesium over the Fukushima region. After reaching the soil surface, radiocesium is quickly bound to fine soil particles. Thereafter, rainfall and snowmelt run-off events transfer particle-bound radiocesium downstream. Characterizing the precipitation regime of the fallout-impacted region is thus important for understanding post-deposition radiocesium dynamics. Accordingly, 10-minute (1995-2015) and daily precipitation data (1977-2015) from 42 meteorological stations within a 100 km radius of the FDNPP were analysed. Monthly rainfall erosivity maps were developed to depict the spatial heterogeneity of rainfall erosivity for catchments entirely contained within this radius. The mean average precipitation in the region surrounding the FDNPP is 1420 mm yr^{-1} (σ 235) with a mean rainfall erosivity of 3696 MJ mm ha^{-1} h^{-1} yr^{-1} (σ 1327). Typhoons contribute 22% of the precipitation (422 mm yr^{-1}) and 40% of the rainfall erosivity (1462 MJ mm ha^{-1} h^{-1} yr^{-1} (σ 637)). The majority of precipitation (60%) and rainfall erosivity (82%) occurs between June and October. At a regional scale, rainfall erosivity increases from the North to the South during July and August, the most erosive months. For the remainder of the year, this gradient occurs mostly from northwest to southeast. Relief features strongly influence the spatial distribution of rainfall erosivity at a smaller scale, with the coastal plains and coastal mountain range having greater rainfall erosivity than the inland, Abukuma river valley. Understanding these patterns, particularly their spatial and temporal (both inter and intra annual) variation, is important for contextualizing soil and particle-bound radiocesium transfers in the Fukushima region. Moreover, understanding the impact of typhoons will be important for managing sediment and sediment-bound contaminant transfers in regions impacted by cyclonic activity.

Key Words: R-Factor, FDNPP, EI_{30}, Erosion, Cesium, typhoon

Author Contributions: J.P.L & L.G-S downloaded and prepared the data, J.P.L and C.C. performed the analyses, all authors were fundamental to drafting and editing the manuscript.

1 Introduction

In March 2011, the Great Tohuku earthquake triggered a giant tsunami that resulted in the Fukushima Dai-ichi nuclear power plant (FDNPP) release of the largest amount of radioactive material since Chernobyl (Chino et al., 2011;Thakur et al., 2013). After the decay of short-lived radionuclides (e.g. ^{131}I, ^{110m}Ag, ^{129}Te), the radionuclide with the most serious short and long term human health concerns is radiocesium ($t_{1/2}$ ^{134}Cs – 2 yr; ^{137}Cs – 30yr) (Kitamura et al., 2014;Saito et al., 2015).

Radiocesium is rapidly bound to fine soil particles and remains stored within the top 0-5cm of the soil profile (Tamura, 1964;Sawhiney, 1972;Kato et al., 2012). As radiocesium is fixated to soil particles in the upper layer of the soil profile, soil erosion and particle transport processes are considered to be the main processes responsible for transferring radiocesium downstream (Saito and Onda, 2015;Yamashiki et al., 2014;Evrard et al., 2015). Rainfall drives erosion by detaching particles from the soil surface, primarily through the kinetic energy of raindrops (Wischmeier and Smith, 1958;Renard and Freimund, 1994). The potential of rainfall to erode soils is referred to as rainfall erosivity. Quantifying rainfall erosivity is important to determine the climatic vulnerability of a region, like Fukushima, to rainfall-driven soil erosion (Mello et al., 2013).

The Universal Soil Loss Equation (USLE) (Wischmeier and Smith, 1978) and its revised edition (RUSLE) (Renard et al., 1997) are some of the most broadly adopted soil erosion modelling frameworks (Oliveira et al., 2013). The USLE predicts average annual soil loss with six factors pertaining to soil, topography, vegetation, management and rainfall erosivity, known as the R-factor. The R-factor estimates rainfall erosivity as a combined function of event duration and intensity (Wischmeier and Smith, 1958). It sums event-based erosivity individually calculated through multiplying each storm's total kinetic energy with its maximum measured 30-minute rainfall intensity. To incorporate variations in inter-annual rainfall, the R-factor is averaged over long temporal periods (~20 years) (Renard and Freimund, 1994;Wischmeier and Smith, 1978).

At many research sites around the world, the R-factor has been found to be highly correlated to soil loss (Ferro et al., 1999;Renard and Freimund, 1994;Wischmeier and Smith, 1958;Wischmeier and Smith, 1978). When all other factors in the (R)USLE are held constant, there is a proportional relationship between soil loss and the R-factor (Lu and Yu, 2002;Wischmeier and Smith, 1958;Wischmeier and Smith, 1978). The utility of the R-factor is

reflected in its global application (McFarlane et al., 1986;Ma et al., 2014;Vrieling et al., 2014;Oliveira et al., 2013;Fiener et al., 2013) including Asia in general (Lee and Heo, 2011;Shamshad et al., 2008;Yu et al., 2001) and Japan in particular (Shiono et al., 2013).

There are limitations with the application of the R-factor and the USLE (Kinnell, 2010). Although the USLE and R-factor were developed from plot scale soil erosion research (Wischmeier and Smith, 1978), they have been applied at the catchment scale (Wilkinson et al., 2009;Kitamura et al., 2014;Belyaev et al., 2005). A debate on the applicability of the USLE within catchment scale modelling frameworks and the universality of the R-factor are beyond the scope of this current research. What is important is that the R-factor and a thorough characterization of the precipitation regime are useful to contextualize local soil erosion, which represents the first step of potential downstream particle-bound contaminant transfers.

Research in the Fukushima region has clearly indicated that precipitation drives downstream radiocesium migration (Evrard et al., 2015). In fact, the majority of soil erosion and concomitant radiocesium migration was reported to coincide with extreme rainfall events (Mouri et al., 2014;Nagao et al., 2013;Onishi et al., 2014). For example, Yamaguchi et al. (2014) reported that most sediment-bound radiocesium migration occurs in flood events that may only occur 1 to 2 times per year. Major typhoons in this region likely transfer significant quantities of radiocesium from hillslopes to the Pacific Ocean (Evrard et al., 2015).

As improved estimates of rainfall erosivity result in more accurate modelling results (Renard et al., 1991;Lee and Heo, 2011), a comprehensive examination of rainfall erosivity, including the impact of typhoons on erosivity, may improve our understanding of sediment and radiocesium dynamics in the Fukushima region. Therefore, the objective of this research is to evaluate the spatial and temporal (monthly and inter-annual) precipitation and rainfall erosivity in general, and from typhoons in particular, for catchments contained entirely within a 100 km radius of the FDNPP accident. Rainfall erosivity maps (monthly and annual) are provided for the Fukushima region along with precipitation and rainfall erosivity data for all events selected by the RUSLE criteria, and information summarizing typhoon and tropical storm events impacting the area since 2011 as supplementary information.

2 Methods:

2.1 Study area

Most of the terrestrial fallout from the FDNPP accident occurred over the coastal catchments of the Fukushima Prefecture (Fig. 1). Soil contamination >25 kBq/kg of $^{134+137}$Cs occurred within small catchments (< 700 km²) draining to the Pacific Ocean, with the highest contamination levels in the coastal mountain range northwest of the FDNPP. The coastal mountain range is separated from the larger westernmost mountain range by the Abukuma river catchment (~5200 km²) extending on a SSW-NNE direction and characterised by a $^{134+137}$C soil contamination <25 kBq/kg.

The region has a humid, subtropical climate along the Pacific coast (Cwa in the Köppen-Geiger climate classification (Peel et al., 2007)), transitioning to a humid continental climate (Dfa) to the west. Based on these classifications, the westward continental region has large differences in seasonal temperatures, with hot and humid summers and cold winters. The subtropical coastal region has slightly warmer winters, along with hot humid summers and more precipitation in the summer months compared to relatively dry winters. There is typhoon driven precipitation in the Fukushima region that results in high volumes and intensities of precipitation occurring during extreme events (Evrard et al., 2014;Chartin et al., 2013). The Japanese typhoon season occurs between May and October with the peak activity occurring between July and September. The mean annual temperature in the Fukushima region is 11.3°C (σ 1.7) ranging from a mean of 0.0 (σ 2.1) in January to 23.4 (σ 1.4) in August.

2.2 Meteorological Stations

All precipitation monitoring stations within a 100 km radius of the FDNPP were analyzed (Fig. 1). Fourteen stations within this 100 km were omitted radius due to an operation period of less than 7 years (n=5) or operation pause during winter months (n=9). Up to 21 years were available for the 10-minute (1995–2015) and 39 years for daily precipitation data (1977–2015) for 42 stations. Daily precipitation was also analyzed from three additional long-term stations (including one located within a 115km radius of the FDNPP) as they had comparable data available from 1890-2015. The long-term stations were excluded from the other analyses owing to high levels of

missing data (μ 33% daily) and short temporal periods (7 years – 10-minute). All data were downloaded from the Japan Meteorological Agency's (JMA) website (http://www.jma.go.jp/jma/index.html).

Daily precipitation data were examined for break points and homogeneity with the RHTest program from the Meteorological Service of Canada (Wang et al., 2010). No significant break points required correction. Duan et al. (2015) similarly did not report significant break points for the JMA daily precipitation data. No homogenization analyses were performed on the 10-minute precipitation data owing the difficulties in assessing heterogeneity in 10-minute precipitation data and the potential to overcorrect the data. Shiono et al. (2013) similarly did not correct 10-minute JMA data. For the daily data, there was an average of only 0.23% of missing data (σ 0.20%, maximum 0.94%) compared to 0.30% (σ 0.20%, maximum 0.78%) for the 10-minute data.

2.3 R-factor calculations

The Rainfall Intensity Summarisation Tool (RIST) software (USDA, 2013) was used to calculate the R-factor, which is a product of the kinetic energy of an event (E) and its maximum 30-minute intensity (I_{30}) (Renard and Freimund, 1994):

$$R = \frac{1}{n}\sum_{j=1}^{n}\sum_{k=1}^{mj}(EI_{30})_k \quad (1)$$

where R equals the annual average rainfall erosivity in MJ mm ha^{-1} hr^{-1} yr^{-1}, n represents the number of years of data utilized, m_j is the number of erosive events in year j, and EI_{30} was calculated as:

$$EI_{30} = \left(\sum_{r=1}^{0} e_r v_r\right) I_{30} \quad (2)$$

with e_r representing the unit energy in MJ ha^{-1} mm^{-1}, v_r is the volume of rainfall (mm) during a given time interval (r), and I_{30} is the maximum rainfall intensity over a 30 minute period of the rainfall event (mm h^{-1}). For each time interval, rainfall energy per unit depth of rainfall (e_r) was calculated as:

$$e_r = 0.29\left[1 - 0.72^{(-0.05 i_r)}\right] \quad (3)$$

with i_r being rainfall intensity (mm h^{-1})(Renard and Freimund, 1994).

To calculate the annual and monthly R-factors, erosive rainfall events were summed for each monitoring station for the considered period (months or year). Two criteria within the RIST software were used to define an erosive event: 1) cumulative rainfall of a given event is >12.7mm; and 2) accumulations <1.27mm over a 6 hour period separates events into two different periods.

To consider the impact of snowfall, precipitation was removed from R-factor calculations when the temperature dropped below 0°C for 31 stations. When removing precipitation that may have occurred as snowfall, there was not a significant difference in the R-factor (t-test p: 0.469) with a mean difference of 26 MJ mm ha^{-1} hr^{-1} yr^{-1} (σ 35). Owing to the limited impact of potential snowfall on R-factor calculations, 11 stations that did not record temperature were included in the analyses.

To examine the impact of typhoons on precipitation and rainfall erosivity, databases of potential typhoon information (i.e., JMA, Wikipedia, Google news) were cross-referenced with regional events that occurred from 1995-2015. This allowed for the quantification of the precipitation and rainfall erosivity that occurred during typhoon related events.

2.4 R-factor spatial analyses

Annual and monthly R-factor data were used to derive maps of annual and monthly rainfall erosivity at a resolution of 250m over the eastern part of the Fukushima Prefecture. Given the number of stations within the investigated area (n=42), a regression approach based on relationships established between the R-factor and spatially distributed covariates was used to produce these maps, rather than interpolation by kriging.

The covariates used for the spatial interpolation of annual and monthly R-factors over the study area are described below:

- Climatic data (i.e. monthly mean precipitation and temperature) from the WorldClim database reported for the period 1950–2000 and with a 30 arc-seconds resolution (equivalent to 1 km resolution) (Hijmans et al., 2005) were used for the monthly models. From the monthly data, annual mean precipitation and temperature were derived to be

included as covariates in the annual R-factor model. These covariates are expected to impact the spatial distribution of rainfall erosivity.

- Based on their known influence on spatial patterns and intensities of rainfall, different morphometric attributes have been included as covariates in the mapping procedure, as proposed by Daly et al. (2002). Precipitation varies strongly with elevation (Barry and Chorley, 2009). Conceptually, relief features can induce different precipitation-elevation gradients depending partially on their ability to block and uplift moisture-bearing air (Daly, 2002). In mountainous areas, the steepest features oriented perpendicular to the air flow are more likely to produce a greater elevation-precipitation gradient than gentle sloping areas parallel to the air flux, such as coastal plains. Moreover, hillslopes experience different climate regimes depending on their orientation, relative to air currents at large scales (i.e., leeward and windward sides of mountains), and solar radiation. Areas located at similar elevations may thus have different precipitation intensities.

  Accordingly, a 90m-resolution Digital Elevation Model (DEM) was extracted from Shuttle Radar Topography Mission (SRTM) of the NASA (Jarvis et al., 2008). Considering the local relief in the fallout affected region (Fig. 1), the DEM was smoothed with a Gaussian filter to two wavelengths of 5 and 20 km. From the 20 km wavelength smoothed DEM, slope and aspect were derived. The slope layer was used in the modelling procedure to account for potential impact of large relief features on moisture-bearing air. The aspect layer derived from the same 20 km wavelength smoothed DEM was used to delineate the opposite sides of mountains and represent leeward and windward sides. Then, this aspect layer was inserted in the model as a categorical covariate (i.e., a 2 values layer, one for each leeward and windward 'facets'). From the 5 km wavelength smoothed DEM, the easting and northing were computed to represent the degree to which aspect is close to the east and the north, respectively (Zar, 2010). These two layers were used as covariates in the modelling procedure to account for slope orientation at a smaller scale than entire side of a mountains range at the coarser scale.

- Distance to the Pacific Ocean coast (DC = distance to the coast) was calculated for each pixel by using the Euclidean distance tool from ArcGis 10 (ESRI, 2011) as the proximity

of the ocean, a major source of moisture, may influence the spatial distribution of precipitation.

Before the fitting of the models, the continuous covariates presented above were rescaled at a 250 m resolution in ArcGIS10 (ESRI, 2011) with bilinear interpolation, that determined the output value of a cell based on a weighted distance average of the four nearest input cell centres. Then, the spatial variation of rainfall erosivity in the study region was modelled with Generalized Additive Models (GAM; Hastie and Tibshirani (1986)), implemented in the mgcv package in R (Wood, 2001). The GAM regression technique is a generalization of linear regression models (GLM) in which the coefficients may be a set of smoothing functions. GAMs consider the non-linearity that may exist between the target variable (Y) and covariates (X) providing more flexibility to the model fitting than a GLM.

As for GLMs, GAMs specify a distribution for the response variable Y and use a link function g relating the conditional mean $\mu(Y)$ of the response variable to an additive function of the selected predictors:

$$g[\mu(Y)] = \alpha + f_1 X_1 + f_2 X_2 + \cdots + f_p X_p \quad (4)$$

where Y is the response variable, X_1, X_2,…X_p represent the covariates and the f_i's the smooth (non-parametric) functions.

Based on monthly and annual mean values for each of the 42 stations, 13 GAMs were fitted to spatially model the R-factor over the study area (i.e. one model per month and one model for the year). A Gaussian distribution model incorporated the conditional mean $\mu(Y)$ and, due to the predominant logarithmic distribution of the monthly and annual data, a log-linear link function $g(\mu) = \log(\mu)$ was implemented. The smoothing functions of the models were built using regression splines fitted by penalized Maximum Likelihood to avoid over-fitting (Wood, 2001). An extra penalty was added to each smoothing term so that each could potentially be set to zero during the fitting process, especially in case of multi-collinearity or multi-concurvity. The interaction of geographical coordinates (longitude and latitude) was then added to each model to consider spatial autocorrelation of the target variable.

A model including all the covariates was first developed (the 'full' model), based on each of the total datasets (13 datasets of n=42). Next, a backward stepwise procedure was applied to select

the appropriate covariates where each of the covariates were sequentially removed from the full model (Poggio et al., 2013;de Brogniez et al., 2015). The AIC (Akaike's Information Criterion; Akaike (1974)) was calculated for the 'full model' and compared with AIC obtained when removing sequentially each of the covariates from the model in order to evaluate the influence of each covariate on the overall capabilities of model prediction.

Explained variance was calculated during the procedure to assess the evolution of 'fitting performance' and to support the decision to keep or remove a covariate into the final model. Once the final model was obtained, a Bayesian approach was used to compute standard errors for the predictions as proposed in the mgcv package. A leave-one-out cross-validation (LOOCV) procedure was applied to each fitted model. Predicted and observed values were compared with the calculation of the Root Mean Square Errors (RMSE) and the coefficient of determination (R^2). Finally, maps were delineated according to the limits of the target area, i.e. entire hydrological basins contained within the 100 km radius of around the FDNPP.

3 Results:

3.1 Spatial and temporal (monthly and inter-annual) precipitation variability

Mean annual precipitation ranged from 1098 mm yr^{-1} at station 281 to 2201 mm yr^{-1} at station 1116 (Table 1; Fig 2A). Mean annual precipitation was 1420 mm yr^{-1} (σ 235 mm yr^{-1})(Fig. 2A) with a coefficient of variation of 17%. 26% (n=11) of the stations plotted outside one standard deviation on the mean, indicative of the spatial heterogeneous precipitation.

Between 1977 and 2015, regional mean annual precipitation ranged from 869 mm in 1984 to 1844 mm in 2006 (Fig. 3A) with a coefficient of variation of 15%. 23% (n=9) of the stations plotted outside one standard deviation on the mean, indicative of high inter-annual variable precipitation. This inter-annual variation in precipitation was maintained over a longer period (Fig. 4) with a mean annual precipitation for the long-term stations (126 yr) being 1159 mm yr^{-1} (σ 187mm) and a 16% coefficient of variation. The 5 year running average for these long-term stations demonstrates that the region experiences prolonged wet and dry periods that last approximately 5 – 10 years. Of note, these long-term stations plot near or below one standard deviation minus the annual precipitation mean for all of the stations, and they therefore may not

be indicative of all precipitation trends in the region. For more a more detailed analysis on long-term trends for precipitation in Japan, see Duan et al. (2015).

The majority of precipitation (60%) occurs between June and October (Fig. 5A) coinciding with a summer wet season that includes periodic typhoons. In fact, 39% of the precipitation occurred between July and September alone, compared to only 22% between March and May, and 17% between November and February. The monthly precipitation also varied spatially. For example, the maximum monthly precipitation average was 318 mm m^{-1} at site 1116 in July compared to 256 mm m^{-1} for site 281 in July.

The highest maximum daily precipitation recorded was 607 mm in 1998 at Site 326, compared to the lowest maximum daily precipitation of 38 mm in 1984 at site 294 (Fig. 6A). The mean maximum daily precipitation was 115 mm (σ 27 mm). The highest mean annual maximum daily precipitation (169 mm) was recorded in 2011 compared to a minimum of 62 mm in 1984. Although the maximum daily precipitation is not an optimal indicator of precipitation depth owing to the probability of events occurring over multiple days, the year of the FDNPP accident (2011), had the highest average daily maximum precipitation as a result of Typhoon Roke.

3.2 Spatial and temporal (monthly and inter-annual) R-factor variability

The annual R-factor ranged from 1972 MJ mm ha^{-1} h^{-1} yr^{-1} at station 290 to 8274 MJ mm ha^{-1} h^{-1} yr^{-1}at station 326 (Table 1 - Fig. 2B). The mean annual R-factor was 3696 MJ mm ha^{-1} h^{-1} yr^{-1} (σ 1327) with a coefficient of variation of 36%. The coefficient of variation was double the corresponding coefficient of variation for annual average precipitation indicative of more spatial variability. 22% (n=11) of the stations plotted outside one standard deviation on the rainfall erosivity mean, equal to that of the annual precipitation.

The regional mean annual R-factor ranged from a minimum of 1866 MJ mm ha^{-1} h^{-1} yr^{-1} in 1996 to a maximum of 7159 MJ mm ha^{-1} h^{-1} yr^{-1} in 1998 (Fig. 3C). The annual R-factor standard deviation was 1252 MJ mm ha^{-1} h^{-1} yr^{-1} with a coefficient of variation of 34%. The coefficient of variation again was more than double than the annual precipitation. 24% (n=5) of years plotted outside one standard deviation of the mean, similar to that of annual precipitation.

The highest monthly R-factors occurred in the summer months and early fall (Fig. 5B) coinciding with the wet summer and the peak typhoon season (July-September). In fact, 82% of the rainfall

298 erosivity occurred between June and October in the Fukushima region, an increase of 22%
299 compared to the amount of precipitation during this period. In particular, 64% of the rainfall
300 erosivity occurs between July and September. Winter (November-February) only contributes 6%
301 of the total annual R-factor with spring (March – May) contributing the remaining 12%.

302 ### 3.3 Annual and monthly rainfall erosivity spatial distribution

303 The deviance explained by the final erosivity models produced by the calibration procedure (from
304 the total dataset of n=42) varied from 82.5% for September to 97.7% for April, and 95.5% for the
305 annual R-factor model (Table 2).

306 Predicted values produced with the LOOCV procedure for the 42 stations showed similar
307 distributions as the observed values (Table 2) for the year and for the months between October
308 and June. For the months between July and September, which includes the typhoon season, the
309 standard deviations of predicted values were smaller than for the observed values. For mean
310 observed values ranging from 778.7 to 799.7 MJ mm ha^{-1} h^{-1} m^{-1} between July and September,
311 the RMSE varied between 165.3 and 313.6 MJ mm ha^{-1} h^{-1} m^{-1} with a R^2 between 0.56 and 0.67.
312 The model fitted for August demonstrated a bias by underestimating R-factor (mean observed
313 values = 778.7 MJ mm ha^{-1} h^{-1} m^{-1} and mean predicted values = 755.2 MJ mm ha^{-1} h^{-1} m^{-1}).

314 For the months between October and June, and for the year, the differences between mean
315 observed and predicted values remained relatively low relative to corresponding observed values
316 and their variability. For these periods, the R^2 produced by the validation procedure varied
317 between 0.62 for April to 0.86 in October, with a R^2 of 0.77 for the annual model.

318 For all of the monthly models, the categorical variable 'facets', was selected as one of the most
319 influential explanatory covariates, whereas facets were less influential in the annual model (Table
320 3). The selection of 'facets' highlights how opposite sides of the mountain ranges in this region
321 have different rainfall erosivity regimes.

322 For 10 of the 13 models, mean precipitation, for the considered period, was selected as a
323 significant explanatory covariate. Mean temperature was selected by the procedure for the three
324 models for which mean precipitation was not retained as significant covariates (i.e., February,
325 November and December). Mean temperature and mean precipitation was selected for the annual
326 R-factor model. According to the ΔAIC, mean precipitation and mean temperature capture the

most R-factor spatial variability within the final models (Table 3). Easting and/or northing were selected in all the other models, except July and September, accounting for the influence of hillslope aspects at smaller scales than entire mountain sides. The selection of elevation, slope and/or the distance to the coast as significant explanatory variables in some of the final models varied.

Although elevation, slope and distance to the coast may influence precipitation patterns and intensities, their non-consistent selection in the final models does not mean that they potentially do not influence rainfall erosivity. Covariates have the potential not to be retained in the final model when there may be multi-collinearity or multi-concurvity between covariates. The non-selection of covariates signifies that other covariates likely have a similar, though stronger, mathematical relationships with the target variable. To achieve parsimony, only select variables from the original set of covariates are included in the final model.

The annual R-factor has a predominantly positive gradient from North North West to South South East (Fig. 7A) and is impacted by the relief of the region. The coastal plain receives lower rainfall erosivity than the adjacent coastal mountain range, both of which have greater rainfall erosivity than the inland Abukuma river valley. The South South East oriented side of the westernmost mountain range bordering the Abukuma valley has lower rainfall erosivity than the easternmost side of this valley. The coefficient of variation (CV) of modelling errors is rather low, predominantly under 10% in the study area (Fig 7B).

In July and August, the most erosive months of the year, rainfall erosivity increases mainly from the North to the South of the region, while during the rest of the year, this gradient occurs mostly from North West to South East. The spatial patterns relative to the relief features are also observed in the monthly rainfall erosivity distributions with the coastal plains and coastal mountain range receiving higher rainfall erosivity than the parallel Abukuma river valley. The maps of errors associated with each monthly R-factor models are available as supplementary information (Fig. S1). The coastal plain and coastal mountainous ranges, including the FDNPP and a large part of the contamination plume with high levels of radiocesium contamination, have greater rainfall erosivity than the less contaminated Abukuma River valley.

3.4 Typhoons

In the Fukushima region, typhoons contributed 22% (331 mm y^{-1}) of the total annual precipitation (Fig 3A). This contribution varies from only 5% (68 mm y^{-1}) in 2003 to 35% (639 mm y^{-1}) in 1998. In September, 60% of the precipitation is derived from typhoon related events (119 mm m^{-1}) compared to 43% in October (64 mm m^{-1}), 28% in August (49 mm m^{-1}) and 25% in July (47 mm m^{-1}). In the remainder of year there is less than a 15 mm m^{-1} contribution from typhoons (<11% of the month precipitation totals)(Fig 5A).

Although typhoons only contribute 22% of the annual precipitation in the region, they contribute 40% of the annual rainfall erosivity (1462 MJ mm ha^{-1} h^{-1} yr^{-1}). This contribution varies from 6% (142 MJ mm ha^{-1} h^{-1} yr^{-1}) in 1995 to 64% in 1998 (4547 MJ mm ha^{-1} h^{-1} yr^{-1})(Fig 3B). In September, 75% of the rainfall erosivity (589 MJ mm ha^{-1} h^{-1} m^{-1}) is derived from typhoon activity, followed by 57% in October (208 MJ mm ha^{-1} h^{-1} m^{-1}), 41% in August (321 mm ha^{-1} h^{-1} m^{-1}), 32% in July (257 mm ha^{-1} h^{-1} m^{-1}), and 19% in June (59 mm ha^{-1} h^{-1} m^{-1})(Fig 5B). Clearly, typhoons contribute a significant amount of rainfall erosivity in the Fukushima region.

4 Discussion:

4.1 Precipitation

The location and intensity of annual typhoons influence the spatial and temporal (intra- and inter-annual) variation in precipitation in the Fukushima region. The majority of precipitation occurs in the summer months, likely the result of the high humidity and residual influences of the seasonal typhoon activity progressing inland. Long-term climatic oscillations (e.g., El Niño) also influence the precipitation patterns, illustrated by the 5–10 year running average reported in the long-term analyses (Duan et al., 2015).

The average precipitation in the Fukushima region (1420 mm yr^{-1}) is ~250 mm less than the mean annual precipitation in Japan (1684 mm yr^{-1})(Kim et al., 2010). Along the western and southeast coast of Japan, annual precipitation may be greater than 3000 mm yr^{-1}(Kim et al., 2010). In the southeast of Japan, the elevated annual precipitation is related to an increasingly tropical climate progressing southwards and the increased occurrence of typhoons in these warmer climates with higher precipitation intensities during summer months.

4.2 Rainfall Erosivity

Similarly to annual precipitation, rainfall erosivity varied spatially and temporally (monthly and inter-annually) in the Fukushima region. Rainfall erosivity also varies in other regions of the world, (e.g. the Mediterranean region (Capolongo et al., 2008) and the Middle East (Eltaif et al., 2010)). Although researchers have demonstrated relationships between precipitation and rainfall erosivity (Ma et al., 2014), in the Fukushima region the relationship was positive, though not significant (r^2 0.39). The lack of significant relationship was likely the result of rainfall erosivity varying more than precipitation. There are also possibly decadal variations in rainfall erosivity, similarly to precipitation, that require long-term analyses to investigate.

There have been a range of R-factors reported for Japan and the Fukushima region. In the Fukushima region, between July 17, 2011 and November 18, 2012, Yoshimura et al. (2015) calculated an R-factor of 3677 MJ mm ha^{-1} h^{-1} (σ 463) for 3 sites near Kawamata town, ~13 km from station 1130. Although station 1130 recorded a similar R-factor for this time period (3853 MJ mm ha^{-1} h^{-1}), the R-factor recorded at this station was 40% lower than the regional average for this period (6559 MJ mm ha^{-1} h^{-1} (σ 3232)). This demonstrates the potential impact of the spatial heterogeneity on rainfall erosivity and limitations of extrapolating data from one sampling point to the entire region.

Yamaguchi et al. (2014) quantified an average annual R-factor of 3366 MJ mm ha^{-1} h^{-1} yr^{-1} for 23 JMA stations in this region for a 10 year period between 2001 and 2011. For a sensitivity analysis, these authors also modelled a maximum case of 4217 MJ mm ha^{-1} h^{-1} yr^{-1} and a minimum case of 1986 MJ mm ha^{-1} h^{-1} yr^{-1}. The average annual R-factor reported by Yamaguchi et al. (2014) was 9% lower than that reported for our current research, likely the result of the longer temporal period and the high levels of rainfall erosivity in the late 1990s not being included in the calculations of Yamaguchi et al. (2014). Further, there was only a 120 MJ mm ha^{-1} h^{-1} yr^{-1} difference between our minimum cases, though our maximum case was 41% higher (7159 MJ mm ha^{-1} h^{-1} yr^{-1}) in 1998 than Yamaguchi et al. (2014), and again 33% higher (6288 MJ mm ha^{-1} h^{-1} yr^{-1}) than their maximum case in 1999.

Around Japan a variety of R-factors have been reported, for example 5880 MJ mm ha^{-1} h^{-1} yr^{-1} in the Onga River basin (Fukuoka prefecture - South Japan)(Tran et al., 2011), 4568 MJ mm ha^{-1} h^{-1} yr^{-1} in the Shiraska River catchment (Aichi prefecture - Central Japan) (Karki and Shibano,

2006), and 2890 MJ mm ha^{-1} h^{-1} yr^{-1} in the Hirose River catchment (Miyagi prefecture - Northern Japan)(Takeuchi and Ishidaira, 2001). Shiono et al. (2013) found that rainfall erosivity varied from 721 to 35299 MJ mm ha^{-1} h^{-1} yr^{-1} across Japan with a mean of 5130 MJ mm ha^{-1} h^{-1} yr^{-1}. In our current analyses, rainfall erosivity in the Fukushima region was found to be similar to the results of Shiono et al. (2013) who spatially depicted rainfall erosivity in the Fukushima region being between 2500 and 5000 MJ mm ha^{-1} h^{-1} yr^{-1}.

Shiono et al. (2013) also demonstrated that rainfall erosivity in the Fukushima region is relatively low compared to the rest of Japan. Similarly to annual precipitation, there is a rainfall erosivity gradient in Japan from north to south, particularly along the Pacific coast with rainfall erosivity increasing southwards from the colder temperate/subarctic regions in the north towards the tropical regions in the south. Importantly, the rainfall erosivity of the Fukushima region is projected, by Shiono et al. (2013), to increase significantly as a result of climate change.

The difference between Shiono et al. (2013) and our current research is the comprehensive analysis of precipitation, and rainfall erosivity at a scale relevant to the fallout from the FDNPP accident. In particular, our current research highlights that the coastal mountain range, which received a significant amount of radiocesium fallout, has higher rainfall erosivity relative to the remainder of the fallout-impacted region, with a large proportion of this rainfall erosivity being derived for typhoons.

4.3 Typhoons

Regions subject to cyclone activity generally have much higher rainfall erosivity. In Mexico, the mean annual rainfall erosivity was 6525 MJ mm ha^{-1} h^{-1} yr^{-1} (García-Oliva et al., 1995). In Peninsular Malaysia, the R-factor was shown to range between 9000 and 14000 MJ mm ha^{-1} h^{-1} yr^{-1} (Shamshad et al., 2008) in one study and between 1360 and 21600 MJ mm ha^{-1} h^{-1} yr^{-1} in another (Yu et al., 2001). In these regions, the majority of the annual precipitation and rainfall erosivity may be derived from only a few storms (García-Oliva et al., 1995). In the Fukushima region, this current research demonstrated that 40% of the rainfall erosivity is derived from typhoons. Accordingly, to model erosion and contaminant transfers in the Fukushima region, it may be important to focus on the spatial distribution of rainfall erosivity from major typhoon events (Chartin et al., in revision).

4.4 Implications for radiocesium dynamics

Precipitation characteristics, such as rainfall erosivity, are fundamental inputs into a variety of approaches to modelling downstream contaminant transfers (Karydas et al., 2015;Yamaguchi et al., 2014;Rosa et al., 1996). Although precipitation and rainfall erosivity alone are insufficient to directly model downstream radiocesium migration, their characterization is important to improve our understanding of radiocesium dynamics. In the Fukushima region, rainfall drives three major contaminant transfer processes: i) wet fallout of particle from the atmosphere to the surface controls the spatial distribution of deposited contaminants, ii) rainfall splash effects trigger the detachment of particle-bound contaminants, and iii) detached particles are potentially transported by overland flow generated by rainfall when infiltration capacity is exceeded or when the soil is saturated with water. In addition, the timing and intensity of events in general, and typhoons in particular, are likely of particular importance for understanding these and other post-fallout radiocesium dynamics in the Fukushima region (Fig 9).

For example, precipitation characteristics occurring immediately after the accident were postulated by Teramage et al. (2014) to account for FDNPP derived radiocesium being reported at 14-16 cm depth in soil cores in samples taken around 10 months after the FDNPP accident. In the Fukushima region, radiocesium has generally been reported to be quickly fixated to soil particles (Matsunaga et al., 2013;Koarashi et al., 2012). Even with this rapid fixation, there have been reports indicating the high precipitation in the region has resulted in the leaching of radiocesium from organic matter (Fujii et al., 2014), and the downward migration of radiocesium in beach sand depth cores (Satou et al., 2015).

The precipitation regime in the Fukushima region has also been postulated to result in the partition between the dissolved and suspended radiocesium loads (K_d) being an order of magnitude higher than reported in riverine systems 1–2 years after Chernobyl (Sakaguchi et al., 2015). In Chernobyl, Sansone et al. (1996) reported that 75% of the radiocesium was transported as a dissolved fraction. In the Fukushima region, the opposite was the case, with the particulate fraction dominating radiocesium transport, particularly during the major typhoon events (for a review see Evrard et al. (2015)).

The Fukushima region has been demonstrated to be highly reactive to major precipitation events (Evrard et al., 2013) with the climate driving a massive and episodic transfer of radiocesium

downstream (Chartin et al., 2013). In fact, Yamaguchi et al. (2014) state that the majority of sediment and radiocesium is transferred downstream in 1–2 major events each year. In Figure 9, the impact of major events is quickly evident. In each year, typhoons contributed rainfall erosivity is greater than the mean monthly rainfall erosivity (individual typhoon and tropical storm data for events since 2011 are presented in Table S1 in the supplementary information). Additionally, there is a significant amount of non-typhoon related erosivity in July and August that may result in significant quantities of radiocesium transfers (Fig. 5B).

The challenge for modelling radiocesium behaviour will be relating the timing of these events to the vegetative cover in the region. This will be particularly important for rice paddy fields which have been suggested to be a significant source of radiocesium transported downstream (Lepage et al., in press). Indeed, incorporating the interaction between rainfall erosivity and landscape cover is fundamental to accurately predicting soil erosion (Evrard et al., 2010). Understanding this interaction between landscape cover and rainfall erosivity is likely even more important in regions subject to intense typhoons such as the Fukushima region, owing to the potential timing of land cover changes (e.g. cultivation cycles such as rice paddy puddling/harvesting) and these major events.

Although the Chernobyl and Fukushima regions have similar humid continental climates (Dfb), the typhoons and other significant summer rainfall events result in a higher precipitation (~2 times) and rainfall erosivity in the Fukushima region (~3–4 times). In the Kharkiv region of Ukraine, the mean annual precipitation is 460 mm y^{-1} (Nazarok et al., 2014), in Odessa it is <500 mm y^{-1} (Svetlitchnyi, 2009) compared to 1420 mm y^{-1} for the Fukushima region. In Ukraine, the region within a 100 km radius from Chernobyl has a rainfall erosivity that ranges from 830 to 1250 MJ mm ha^{-1} h^{-1} y^{-1} (Larionov, 1993). Within 100 km from the FDNPP accident, the R factor is ~3 to 4 times higher (3696 MJ mm ha^{-1} h^{-1} y^{-1}). As there is positive relationship between rainfall erosivity and soil loss, where other factors are held equal, higher erosion rates and therefore a more rapid radiocesium export is anticipated in the Fukushima region compared to Chernobyl, based on these differences in their climatic contexts.

The provision of the R-factor maps focusing on the region impacted by fallout from the FDNPP accident that depict the annual and monthly variation in the R-factor are important to inform management and support the research and modelling of radiocesium dynamics in this region.

These R-factor maps are thus provided to the community (Dataset 1). Further, all the event data (total precipitation, rainfall erosivity and kinetic energy) are included in the supplementary information (Dataset 2). More research is nevertheless required to examine the impact of different rain drop size distributions and resultant variations in kinetic energy in this region.

5 Conclusions

Rainfall erosivity in the Fukushima region is 3696 MJ mm ha^{-1} h^{-1} yr^{-1} and the region receives 1420 mm y^{-1} of precipitation. Although these are below average values for Japan, the rainfall erosivity is more than 3–4 times higher than in Chernobyl. The majority of precipitation (60%) and rainfall erosivity (86%) occurs between June and October. Major typhoon events are responsible for 22% of the precipitation (422 mm yr^{-1}) and 40% of the rainfall erosivity (1462 MJ mm ha^{-1} h^{-1} yr^{-1} (σ 637)). The highest areas of contamination in the coastal mountain range correspond to the contaminated area that receives high rainfall erosivity.

The R-factor maps demonstrate that areas most contaminated with radiocesium with the highest rainfall erosivity are located along in coastal mountain range of the Pacific Ocean west of the FDNPP. Catchments in these areas will have the highest sensitivity to rainfall induced soil erosion and thus potential concomitant radiocesium transfers to downstream catchments and ultimately to the Pacific Ocean. The highest rainfall erosivity in these areas occurs during the typhoon season (July-September). Monitoring radiocesium transfers after major events will be important. In other catchments that may be impacted by future radiocesium contamination it will be important to similarly investigate the climatic context, as precipitation strongly influences post-fallout radiocesium dynamics.

Acknowledgements

We would like to thank three reviewers for their constructive comments that helped improve this manuscript. This research was funded by the ANR (*French National Research Agency*) in the framework of the AMORAD project (ANR-11-RSNR-0002).

References

Akaike, H.: A new look at the statistical model identification, Automatic Control, IEEE Transactions on, 19, 716-723, 1974.

Barry, R. G., and Chorley, R. J.: Atmosphere, weather and climate, Routledge, 2009.

Belyaev, V. R., Golosov, V. N., Ivanova, N. N., Markelov, M. V., and Tishkina, E. V.: Human-accelerated soil redistribution within an intensively cultivated dry valley catchment in southern European Russia, Iahs-Aish P, 291, 11-20, 2005.

Capolongo, D., Diodato, N., Mannaerts, C. M., Piccarreta, M., and Strobl, R. O.: Analyzing temporal changes in climate erosivity using a simplified rainfall erosivity model in Basilicata (southern Italy), Journal of Hydrology, 356, 119-130, http://dx.doi.org/10.1016/j.jhydrol.2008.04.002, 2008.

Chartin, C., Evrard, O., Onda, Y., Patin, J., Lefèvre, I., Ottlé, C., Ayrault, S., Lepage, H., and Bonté, P.: Tracking the early dispersion of contaminated sediment along rivers draining the Fukushima radioactive pollution plume, Anthropocene, 1, 23-34, 2013.

Chartin, C., Evrard, O., Onda, Y., Laceby, P., Cerdan, O., Lepage, H., Ottlé, C., Lefèvre, I., and Bonté, P.: The impact of typhoons on sediment connectivity: Lessons learnt from contaminated coastal catchments of Fukushima Prefecture (Japan), Earth Surface Processes and Landforms, in revision.

Chino, M., Nakayama, H., Nagai, H., Terada, H., Katata, G., and Yamazawa, H.: Preliminary estimation of release amounts of ^{131}I and ^{137}Cs accidentally discharged from the Fukushima Daiichi nuclear power plant into the atmosphere, Journal of nuclear science and technology, 48, 1129-1134, 2011.

Daly, C.: Variable influence of terrain on precipitation patterns: Delineation and use of effective terrain height in PRISM, World Wide Web document. http://www. ocs. orst. edu/prism/effter. pdf, 2002.

Daly, C., Gibson, W. P., Taylor, G. H., Johnson, G. L., and Pasteris, P.: A knowledge-based approach to the statistical mapping of climate, Climate research, 22, 99-113, 2002.

de Brogniez, D., Ballabio, C., Stevens, A., Jones, R., Montanarella, L., and van Wesemael, B.: A map of the topsoil organic carbon content of Europe generated by a generalized additive model, European Journal of Soil Science, 66, 121-134, 2015.

Duan, W., He, B., Takara, K., Luo, P., Hu, M., Alias, N. E., and Nover, D.: Changes of precipitation amounts and extremes over Japan between 1901 and 2012 and their connection to climate indices, Climate Dynamics, 45, 2273-2292, 2015.

Eltaif, N. I., Gharaibeh, M. A., Al-Zaitawi, F., and Alhamad, M. N.: Approximation of Rainfall Erosivity Factors in North Jordan, Pedosphere, 20, 711-717, http://dx.doi.org/10.1016/S1002-0160(10)60061-6, 2010.

ESRI: ArcGIS Desktop: Release 10, in, Redlands. Environmental Systems Research Institute, CA, 2011.

Evrard, O., Nord, G., Cerdan, O., Souchère, V., Le Bissonnais, Y., and Bonté, P.: Modelling the impact of land use change and rainfall seasonality on sediment export from an agricultural catchment of the northwestern European loess belt, Agriculture, Ecosystems & Environment, 138, 83-94, 2010.

Evrard, O., Chartin, C., Onda, Y., Patin, J., Lepage, H., Lefèvre, I., Ayrault, S., Ottlé, C., and Bonté, P.: Evolution of radioactive dose rates in fresh sediment deposits along coastal rivers draining Fukushima contamination plume, Scientific reports, 3, 2013.

566 Evrard, O., Chartin, C., Onda, Y., Lepage, H., Cerdan, O., Lefevre, I., and Ayrault, S.: Renewed soil erosion
567 and remobilisation of radioactive sediment in Fukushima coastal rivers after the 2013 typhoons, Sci.
568 Rep., 4, 10.1038/srep04574, 2014.

569 Evrard, O., Laceby, J. P., Lepage, H., Onda, Y., Cerdan, O., and Ayrault, S.: Radiocesium transfer from
570 hillslopes to the Pacific Ocean after the Fukushima Nuclear Power Plant accident: A review, Journal of
571 Environmental Radioactivity, 148, 92-110, http://dx.doi.org/10.1016/j.jenvrad.2015.06.018, 2015.

572 Ferro, V., Porto, P., and Yu, B.: A comparative study of rainfall erosivity estimation for southern Italy and
573 southeastern Australia, Hydrological Sciences Journal, 44, 3-24, 10.1080/02626669909492199, 1999.

574 Fiener, P., Neuhaus, P., and Botschek, J.: Long-term trends in rainfall erosivity–analysis of high resolution
575 precipitation time series (1937–2007) from Western Germany, Agricultural and Forest Meteorology,
576 171–172, 115-123, http://dx.doi.org/10.1016/j.agrformet.2012.11.011, 2013.

577 Fujii, K., Ikeda, S., Akama, A., Komatsu, M., Takahashi, M., and Kaneko, S.: Vertical migration of
578 radiocesium and clay mineral composition in five forest soils contaminated by the Fukushima nuclear
579 accident, Soil Science and Plant Nutrition, 60, 751-764, 2014.

580 García-Oliva, F., Maass, J. M., and Galicia, L.: Rainstorm Analysis and Rainfall Erosivity of a Seasonal
581 Tropical Region with a Strong Cyclonic Influence on the Pacific Coast of Mexico, Journal of Applied
582 Meteorology, 34, 2491-2498, 10.1175/1520-0450(1995)034<2491:RAAREO>2.0.CO;2, 1995.

583 Hastie, T., and Tibshirani, R.: Generalized additive models, Statistical science, 297-310, 1986.

584 Hijmans, R. J., Cameron, S. E., Parra, J. L., Jones, P. G., and Jarvis, A.: Very high resolution interpolated
585 climate surfaces for global land areas, International journal of climatology, 25, 1965-1978, 2005.

586 Jarvis, A., Reuter, H. I., Nelson, A., and Guevara, E.: Hole-filled SRTM for the globe Version 4, available
587 from the CGIAR-CSI SRTM 90m Database (http://srtm. csi. cgiar. org), 2008.

588 Karki, K. B., and Shibano, H.: Soil loss in a forested watershed underlain by deeply weathered granite:
589 comparison of observations to predictions of a GIS-based USLE, Bulletin of the Tokyo University Forests,
590 2006.

591 Karydas, C. G., Tzoraki, O., and Panagos, P.: A New Spatiotemporal Risk Index for Heavy Metals:
592 Application in Cyprus, Water, 7, 4323-4342, 2015.

593 Kato, H., Onda, Y., and Teramage, M.: Depth distribution of 137Cs, 134Cs, and 131I in soil profile after
594 Fukushima Dai-ichi Nuclear Power Plant Accident, Journal of Environmental Radioactivity, 111, 59-64,
595 http://dx.doi.org/10.1016/j.jenvrad.2011.10.003, 2012.

596 Kim, S., Nakakita, E., Tachikawa, Y., and Takara, K.: Precipitation changes in Japan under the A1B climate
597 change scenario, Annual Journal of Hydraulic Engineering, JSCE, 54, 127-132, 2010.

598 Kinnell, P. I. A.: Event soil loss, runoff and the Universal Soil Loss Equation family of models: A review,
599 Journal of Hydrology, 385, 384-397, http://dx.doi.org/10.1016/j.jhydrol.2010.01.024, 2010.

600 Kitamura, A., Yamaguchi, M., Kurikami, H., Yui, M., and Onishi, Y.: Predicting sediment and cesium-137
601 discharge from catchments in eastern Fukushima, Anthropocene, 5, 22-31,
602 http://dx.doi.org/10.1016/j.ancene.2014.07.001, 2014.

603 Koarashi, J., Atarashi-Andoh, M., Matsunaga, T., Sato, T., Nagao, S., and Nagai, H.: Factors affecting
604 vertical distribution of Fukushima accident-derived radiocesium in soil under different land-use
605 conditions, Science of the Total Environment, 431, 392-401, 2012.

606 Larionov, G.: Erosion and deflation of soils, in, Moscow University Press. Moscow, Russia (in Russian),
607 pp200, 1993.

608 Lee, J.-H., and Heo, J.-H.: Evaluation of estimation methods for rainfall erosivity based on annual
609 precipitation in Korea, Journal of Hydrology, 409, 30-48,
610 http://dx.doi.org/10.1016/j.jhydrol.2011.07.031, 2011.

611 Lepage, H., Laceby, J. P., Bonté, P., Joron, J.-L., Onda, Y., Lefèvre, I., Ayrault, S., and Evrard, O.:
612 Investigating the source of radiocesium contaminated sediment in two Fukushima coastal catchments
613 with sediment tracing techniques, Anthropocene, in press.

614 Lu, H., and Yu, B.: Spatial and seasonal distribution of rainfall erosivity in Australia, Soil Research, 40, 887-
615 901, 2002.

616 Ma, X., He, Y., Xu, J., van Noordwijk, M., and Lu, X.: Spatial and temporal variation in rainfall erosivity in a
617 Himalayan watershed, CATENA, 121, 248-259, http://dx.doi.org/10.1016/j.catena.2014.05.017, 2014.

618 Matsunaga, T., Koarashi, J., Atarashi-Andoh, M., Nagao, S., Sato, T., and Nagai, H.: Comparison of the
619 vertical distributions of Fukushima nuclear accident radiocesium in soil before and after the first rainy
620 season, with physicochemical and mineralogical interpretations, Science of the Total Environment, 447,
621 301-314, 2013.

622 McFarlane, D., Westcott, T., and Davies, J.: Rainfall erosivity in Western Australia, Hydrology and Water
623 Resources Symposium 1986: River Basin Management; Preprints of Papers, 1986, 350,

624 Mello, C. R., Viola, M. R., Beskow, S., and Norton, L. D.: Multivariate models for annual rainfall erosivity in
625 Brazil, Geoderma, 202–203, 88-102, http://dx.doi.org/10.1016/j.geoderma.2013.03.009, 2013.

626 Mouri, G., Golosov, V., Shiiba, M., and Hori, T.: Assessment of the caesium-137 flux adsorbed to
627 suspended sediment in a reservoir in the contaminated Fukushima region in Japan, Environmental
628 Pollution, 187, 31-41, http://dx.doi.org/10.1016/j.envpol.2013.12.018, 2014.

629 Nagao, S., Kanamori, M., Ochiai, S., Tomihara, S., Fukushi, K., and Yamamoto, M.: Export of ^{134}Cs and
630 ^{137}Cs in the Fukushima river systems at heavy rains by Typhoon Roke in September 2011, Biogeosciences
631 Discuss., 10, 2767-2790, 10.5194/bgd-10-2767-2013, 2013.

632 Nazarok, P., Kruglov, O., Menshov, O., Kutsenko, M., and Sukhorada, A.: Mapping soil erosion using
633 magnetic susceptibility. A case study in Ukraine, Solid Earth Discussions, 6, 831-848, 2014.

634 Oliveira, P. T. S., Wendland, E., and Nearing, M. A.: Rainfall erosivity in Brazil: A review, CATENA, 100,
635 139-147, http://dx.doi.org/10.1016/j.catena.2012.08.006, 2013.

636 Onishi, Y., Kurikami, H., and Yokuda, S.: Simulation of Sediment and Cesium Transport in the Ukedo River
637 and the Ogi Dam Reservoir during a Rainfall Event using the TODAM Code, Pacific Northwest National
638 Laboratory (PNNL), Richland, WA (US), 2014.

639 Peel, M. C., Finlayson, B. L., and McMahon, T. A.: Updated world map of the Köppen-Geiger climate
640 classification, Hydrology and earth system sciences discussions, 4, 439-473, 2007.

641 Poggio, L., Gimona, A., and Brewer, M. J.: Regional scale mapping of soil properties and their uncertainty
642 with a large number of satellite-derived covariates, Geoderma, 209, 1-14, 2013.

643 Renard, K. G., Foster, G. R., Weesies, G. A., and Porter, J. P.: RUSLE: Revised universal soil loss equation,
644 Journal of soil and Water Conservation, 46, 30-33, 1991.

Renard, K. G., and Freimund, J. R.: Using monthly precipitation data to estimate the R-factor in the revised USLE, Journal of Hydrology, 157, 287-306, http://dx.doi.org/10.1016/0022-1694(94)90110-4, 1994.

Renard, K. G., Foster, G. R., Weesies, G. A., McCool, D., and Yoder, D.: Predicting soil erosion by water: a guide to conservation planning with the revised universal soil loss equation (RUSLE), Agriculture Handbook (Washington), 1997.

Rosa, D. d. l., Crompvoets, J., Mayol Rodríguez, F., and Moreno Arce, J. A.: Land vulnerability evaluation and climate change impacts in Andalucia, Spain: soil erosion and contamination, 1996.

Saito, K., and Onda, Y.: Outline of the national mapping projects implemented after the Fukushima accident, Journal of environmental radioactivity, 139, 240-249, 2015.

Saito, K., Tanihata, I., Fujiwara, M., Saito, T., Shimoura, S., Otsuka, T., Onda, Y., Hoshi, M., Ikeuchi, Y., and Takahashi, F.: Detailed deposition density maps constructed by large-scale soil sampling for gamma-ray emitting radioactive nuclides from the Fukushima Dai-ichi Nuclear Power Plant accident, Journal of environmental radioactivity, 139, 308-319, 2015.

Sakaguchi, A., Tanaka, K., Iwatani, H., Chiga, H., Fan, Q., Onda, Y., and Takahashi, Y.: Size distribution studies of ^{137}Cs in river water in the Abukuma Riverine system following the Fukushima Dai-ichi Nuclear Power Plant accident, Journal of Environmental Radioactivity, 139, 379–389, 2015.

Sansone, U., Belli, M., Voitsekovitch, O. V., and Kanivets, V. V.: ^{137}Cs and ^{90}Sr in water and suspended particulate matter of the Dnieper River-Reservoirs System (Ukraine), Science of the Total Environment, 186, 257-271, 1996.

Satou, Y., Sueki, K., Sasa, K., Kitagawa, J.-i., Ikarashi, S., and Kinoshita, N.: Vertical distribution and formation analysis of the ^{131}I, ^{137}Cs, ^{129m}Te, and ^{110m}Ag from the Fukushima Dai-ichi Nuclear Power Plant in the beach soil, J Radioanal Nucl Ch, 303, 1197-1200, 2015.

Sawhiney, B.: Selective sorption and fixation of cations by clay minerals: a review, Clays Clay Miner, 20, 93-100, 1972.

Shamshad, A., Azhari, M. N., Isa, M. H., Hussin, W. M. A. W., and Parida, B. P.: Development of an appropriate procedure for estimation of RUSLE EI30 index and preparation of erosivity maps for Pulau Penang in Peninsular Malaysia, CATENA, 72, 423-432, http://dx.doi.org/10.1016/j.catena.2007.08.002, 2008.

Shiono, T., Ogawa, S., Miyamoto, T., and Kameyama, K.: Expected impacts of climate change on rainfall erosivity of farmlands in Japan, Ecological Engineering, 61, 678-689, 2013.

Svetlitchnyi, A.: Soil Erosion Induced Degradation of Agrolandscapes in Ukraine: Modeling, Computation and Prediction in Conditions of the Climate Changes, in: Regional Aspects of Climate-Terrestrial-Hydrologic Interactions in Non-boreal Eastern Europe, edited by: Groisman, P., and Ivanov, S., NATO Science for Peace and Security Series C: Environmental Security, Springer Netherlands, 191-199, 2009.

Takeuchi, B. K., and Ishidaira, H.: The examination of sediment production estimation by the USLE method in mountainous basins of Japan, Hydraulic Engineering, 45, 85-90, 2001.

Tamura, T.: Consequences of activity release: selective sorption reactions of cesium with soil minerals, Nuclear Safety 5, 262–268, 1964.

Teramage, M. T., Onda, Y., Patin, J., Kato, H., Gomi, T., and Nam, S.: Vertical distribution of radiocesium in coniferous forest soil after the Fukushima nuclear power plant accident, Journal of environmental radioactivity, 137, 37-45, 2014.

Thakur, P., Ballard, S., and Nelson, R.: An overview of Fukushima radionuclides measured in the northern hemisphere, Science of The Total Environment, 458–460, 577-613, http://dx.doi.org/10.1016/j.scitotenv.2013.03.105, 2013.

Tran, T. A., Mitani, Y., Ikemi, H., and Matsuki, H.: Human Impacts on Erosion and Deposition in Onga River Basin, Kyushu, Japan, Memoirs of the Faculty of Engineering, Kyushu University, 71, 47-65, 2011.

USDA: Rainfall Intensity Summarization Tool (RIST), United States Department of Agriculture (USDA), Agriculture Research Service, National Sedimentation Laboratory, Oxford, Mississippi, Version 3.88, in, 2013.

Vrieling, A., Hoedjes, J. C. B., and van der Velde, M.: Towards large-scale monitoring of soil erosion in Africa: Accounting for the dynamics of rainfall erosivity, Global Planet Change, 115, 33-43, http://dx.doi.org/10.1016/j.gloplacha.2014.01.009, 2014.

Wang, X. L., Chen, H., Wu, Y., Feng, Y., and Pu, Q.: New Techniques for the Detection and Adjustment of Shifts in Daily Precipitation Data Series, Journal of Applied Meteorology and Climatology, 49, 2416-2436, 10.1175/2010JAMC2376.1, 2010.

Wilkinson, S. N., Prosser, I. P., Rustomji, P., and Read, A. M.: Modelling and testing spatially distributed sediment budgets to relate erosion processes to sediment yields, Environment Modelling and Software, 24, 489-501, 2009.

Wischmeier, W. H., and Smith, D. D.: Rainfall energy and its relationship to soil loss, Transactions American Geophysical Union, 39, 285-291, 10.1029/TR039i002p00285, 1958.

Wischmeier, W. H., and Smith, D. D.: Predicting rainfall erosion losses-A guide to conservation planning, Predicting rainfall erosion losses-A guide to conservation planning, 1978.

Wood, S. N.: mgcv: GAMs and generalized ridge regression for r. R news, 1(2), 2-25, 2001.

Yamaguchi, M., Kitamura, A., Oda, Y., and Onishi, Y.: Predicting the long-term ^{137}Cs distribution in Fukushima after the Fukushima Dai-ichi nuclear power plant accident: a parameter sensitivity analysis, Journal of Environmental Radioactivity, 135, 135-146, http://dx.doi.org/10.1016/j.jenvrad.2014.04.011, 2014.

Yamashiki, Y., Onda, Y., Smith, H. G., Blake, W. H., Wakahara, T., Igarashi, Y., Matsuura, Y., and Yoshimura, K.: Initial flux of sediment-associated radiocesium to the ocean from the largest river impacted by Fukushima Daiichi Nuclear Power Plant, Scientific Reports, 4, 10.1038/srep03714, 2014.

Yoshimura, K., Onda, Y., and Kato, H.: Evaluation of radiocaesium wash-off by soil erosion from various land uses using USLE plots, Journal of Environmental Radioactivity, 139, 362–369, http://dx.doi.org/10.1016/j.jenvrad.2014.07.019, 2015.

Yu, B., Hashim, G., and Eusof, Z.: Estimating the R-factor with limited rainfall data: a case study from peninsular Malaysia, Journal of Soil and Water Conservation, 56, 101-105, 2001.

Zar, J. H.: Biostatistical Analysis, in, 5th Edition ed., Prentice Hall, New Jersey, 944, 2010.

Table 1. Station coordinates along with the annual precipitation, R-Factor and kinetic energy (KE) mean and standard deviation (S.D.).

Station	Latitude	Longitude	Annual Precipitation (mm)		R-Factor (MJ mm^{-1} ha^{-1} h^{-1} yr^{-1})		KE (MJ ha^{-1} yr^{-1})	
			Mean	S.D.	Mean	S.D.	Mean	S.D.
254[A-4]	38.178	140.635	1429	302	3295	3045	167	61
256	38.015	140.612	1292	243	2497	1296	149	42
257	38.025	140.858	1256	259	2922	1313	148	38
279	37.912	140.143	1343	221	2049	572	142	28
281	37.852	140.588	1098	172	2045	792	121	26
285	37.783	140.925	1350	266	3859	1928	171	48
288^	37.638	140.983	1333	272	3819	1527	173	39
290	37.552	140.108	1265	242	1972	1029	124	35
291	37.583	140.430	1176	219	2337	1206	136	33
294	37.435	140.577	1168	210	2718	1355	141	36
295	37.492	140.965	1493	299	4327	1694	196	43
299	37.368	140.330	1154	176	2465	982	130	30
300^[D]	37.347	141.017	1532	295	4249	1517	203	40
304	37.287	140.625	1231	200	2984	1361	145	31
307	37.147	140.460	1280	205	3405	1530	157	34
310^	37.065	140.877	1426	281	4425	2105	193	49
312	36.938	140.408	1399	234	4342	2145	182	46
314^	36.868	140.637	2001	380	7177	2405	274	55
315	36.833	140.772	1472	247	4126	1629	185	42
316[10]	36.778	140.345	1419	204	5075	2370	193	39
326	37.123	140.035	1954	373	8274	8491	279	78
1011	36.580	140.645	1474	232	4406	2002	191	37
1034	37.233	141.000	1568	280	4530	1545	205	45
1116[3]	37.668	140.260	2201	355	5056	2385	262	57
1127[c-6]	37.008	140.737	1435	285	3636	1263	178	46
1129	37.337	140.808	1444	250	4193	2115	185	42
1130	37.695	140.747	1307	245	2989	1563	157	41
1132[10]	38.003	140.207	1254	199	2350	1380	127	34
1150^[10]	37.560	140.753	1341	239	3470	1369	165	35
1173^[10]	36.778	140.482	1437	234	4432	1981	191	42
1220[10]	37.932	140.778	1262	245	2878	1234	149	40
1268^[8]	37.288	140.218	1366	256	3680	2595	170	50
1274^[8]	37.207	140.750	1440	272	4156	1812	181	43
1282[9]	37.722	140.058	1762	316	3351	1764	200	49
1293[9]	37.892	140.437	1363	178	2361	916	144	29
1294[9]	37.277	140.063	1568	281	3914	2567	190	51
1298^[8]	37.827	140.728	1462	270	3765	2209	175	46
1386^[7]	37.388	140.090	1311	231	2726	1569	142	39
1421^[5]	36.743	140.593	1851	284	6448	2422	249	50
1464	38.138	140.917	1129	174	2742	1522	133	27
1466[B-2]	37.227	140.427	1232	213	3150	1055	146	33
1564	38.127	140.680	1356	170	2647	1030	154	26

^No temperature data available

[A] For R-factor, 10 years of data available, [B] 13y, [C] 14y, [D]18y

[1]For precipitation analyses, 10y available, [2] 13y, [3] 21y, [4] 28y, [5] 30y, [6] 32y, [7] 33y, [8] 36 y, [9] 37 y, [10] 38y

Table 2. Observed and predicted mean and standard deviation (S.D.) for monthly (in MJ mm ha^{-1} h^{-1} m^{-1}) and annual R-factors (in MJ mm ha^{-1} h^{-1} yr^{-1}) with GAM performance parameters (RMSE: Root Mean Square Error; R^2: coefficient of determination).

Month or Year	Observed R		Predicted R		Deviance explained	Model performance (LOOCV)	
	Mean	S.D.	Mean	S.D.	(%)	RMSE	R^2
Year	3696	1327	3696	1293	95.5	640	0.77
January	43.1	25.8	44.2	25.4	89.6	12.7	0.77
Februray	23.7	16.0	23.0	15.0	90.3	9.2	0.68
March	63.5	31.2	63.7	30.1	93.4	12.9	0.83
April	160.1	103.9	165.1	97.2	92.4	66.0	0.62
May	206.1	159.9	213.5	163.0	97.7	75.2	0.80
June	311.6	124.4	312.1	116.2	87.6	65.9	0.72
July	799.7	283.1	800.3	243.9	83.2	167.4	0.65
August	778.7	469.0	755.2	304.6	92.4	313.6	0.56
September	785.2	287.0	780.9	263.4	82.5	165.3	0.67
October	367.6	246.6	373.8	237.4	95.2	92.4	0.86
November	73.1	27.7	72.2	24.9	90.4	12.4	0.80
December	83.4	66.3	84.3	62.1	93.2	32.6	0.76

725

Table 3. Results from the backward stepwise procedure used to select covariates to include in final GAMs for annual and monthly R-factor maps computation. The values (ΔAIC) correspond to the difference in AIC scores obtained when the particular covariate is dropped from the 'full' model, i.e., the model containing all the covariates. Scores in bold indicate which covariates were selected in the final models.

Model	ΔAIC							
	Elevation	Slope	DC*	Easting	Northing	Rainfall	Temperature	Facets
Annual	**8.7**	1.0	**10.8**	**12.1**	2.8	**13.6**	**10.1**	**5.6**
January	0.0	**6.1**	**2.1**	**0.7**	0.0	**8.3**	0.0	**4.0**
February	**2.2**	0.0	0.1	**2.7**	**2.6**	0.2	**4.6**	**8.6**
March	0.0	**9.9**	0.0	**1.3**	0.1	**5.3**	0.0	**3.2**
April	**3.7**	0.0	**17.6**	0.0	**0.5**	**17.3**	0.0	**14.0**
May	0.1	**8.5**	0.0	**0.7**	**4.5**	**8.4**	0.0	**10.9**
June	0.4	0.3	0.0	0.2	**1.4**	**8.6**	0.0	**12.6**
July	0.0	0.3	**5.5**	0.0	0.0	**13.2**	0.0	**13.8**
August	**0.7**	**1.6**	0.0	0.0	**8.6**	**8.8**	0.1	**7.8**
September	0.0	0.4	**5.5**	0.0	0.0	**13.2**	0.0	**13.8**
October	0.4	**4.8**	**1.2**	0.0	**5.7**	**16.3**	0.0	**19.8**
November	0.0	**26.3**	**2.7**	**3.0**	0.2	0.2	**11.2**	**8.8**
December	0.3	0.2	0.0	**3.2**	0.4	0.6	**11.7**	**5.5**

* Distance to Coast

733

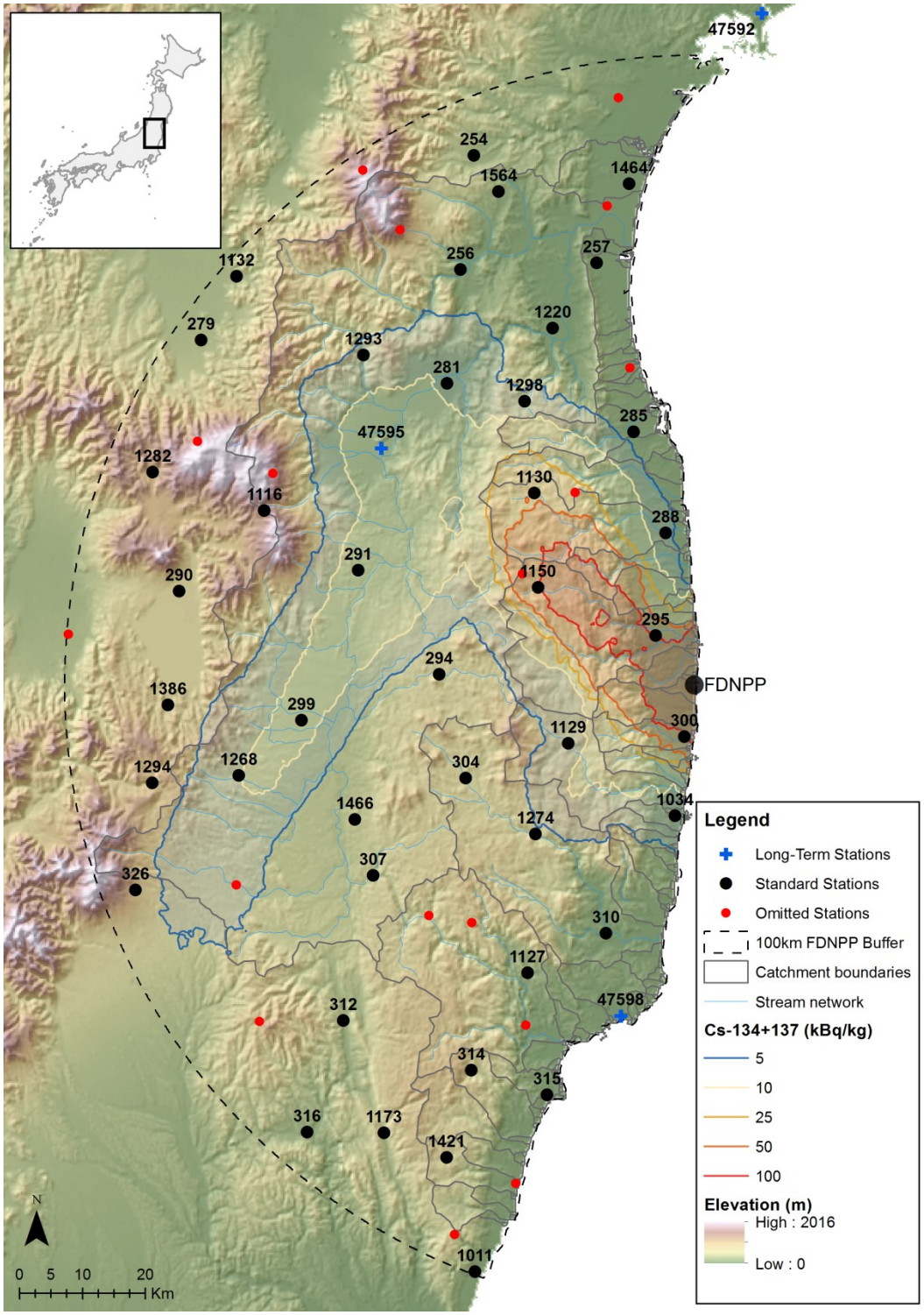

Figure 1. Standard, omitted and long-term stations in the Fukushima region, along with catchments (grey lines) contained entirely within a 100km buffer around the FDNPP (dashed line) $^{134+137}$Cs activities are from Chartin et al. (2013)

734

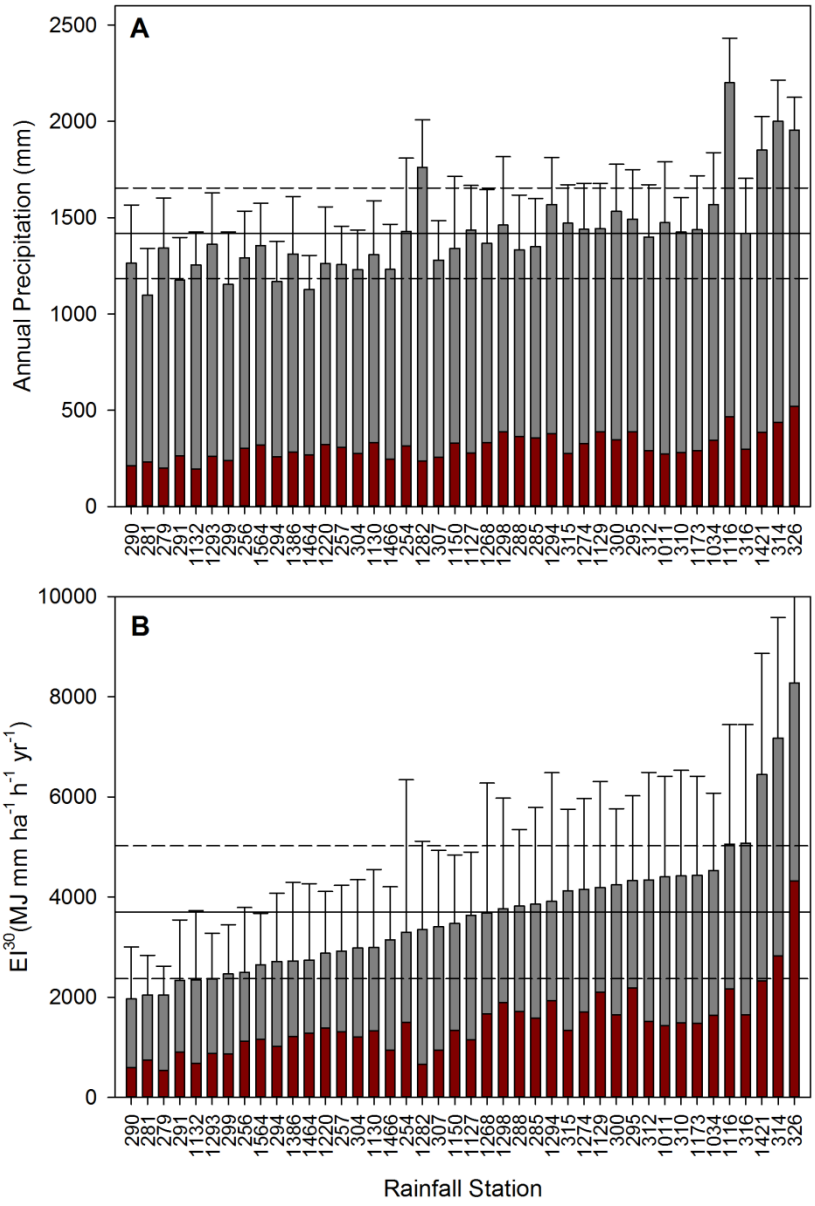

Figure 2. Total (grey) and typhoon-related (red) mean annual precipitation (A-Top) and R-factor (B-Bottom) with the solid line representing the mean and the dashed lines being one standard deviation on the mean. The error bars indicate one standard deviation on the mean for individual stations.

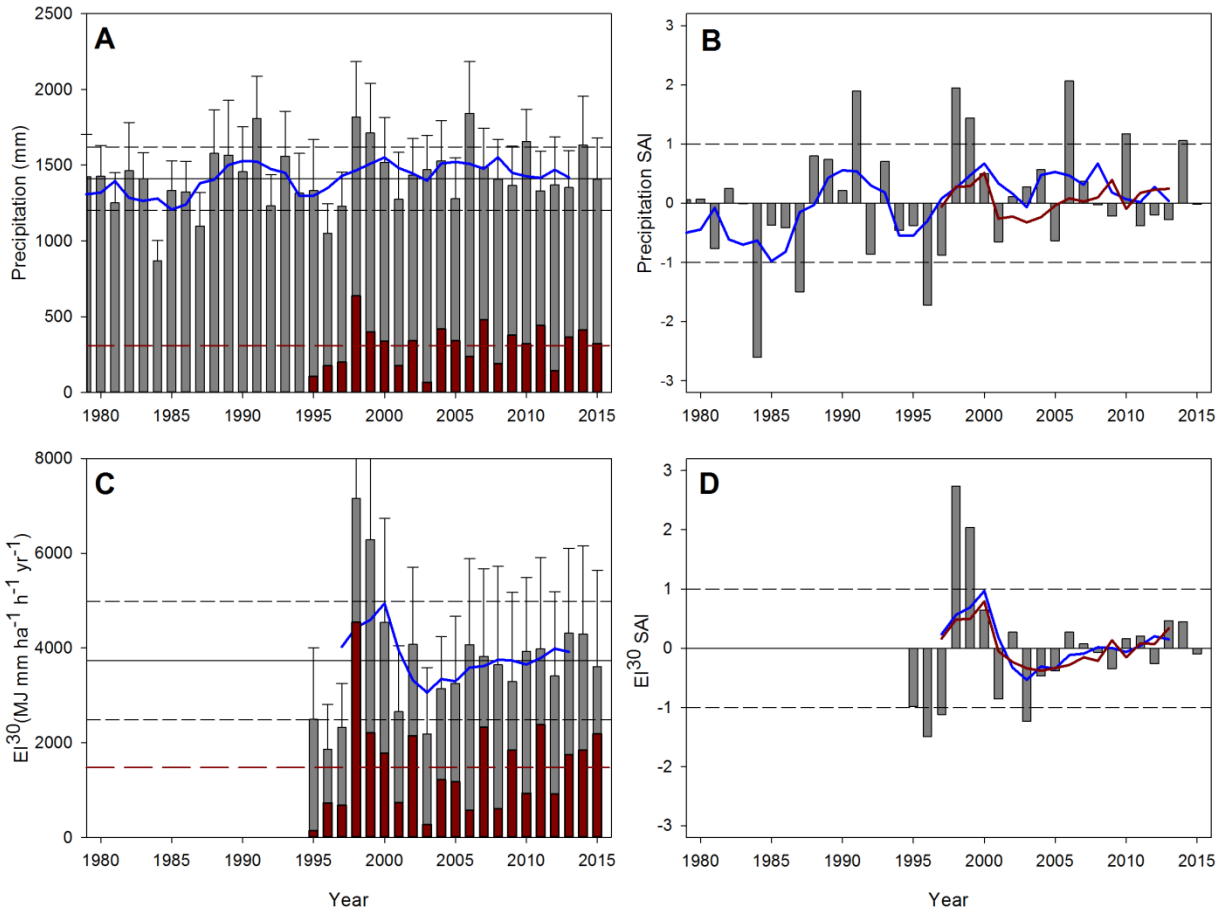

Figure 3. Annual (grey) and typhoon-related (red) mean annual precipitation (A) and corresponding standardized anomaly index (SAI – B) and the annul (grey) and typhoon related (red) R-factor (C) and the R-factor's SAI (D). The grey solid line represent the regional mean (including typhoons) and the grey dashed lines represent one standard deviation on the total mean whereas the red dashed line representing the mean contribution from typhoon events. The blue (total) and red (typhoon) solid lines depict the 5-year running average.

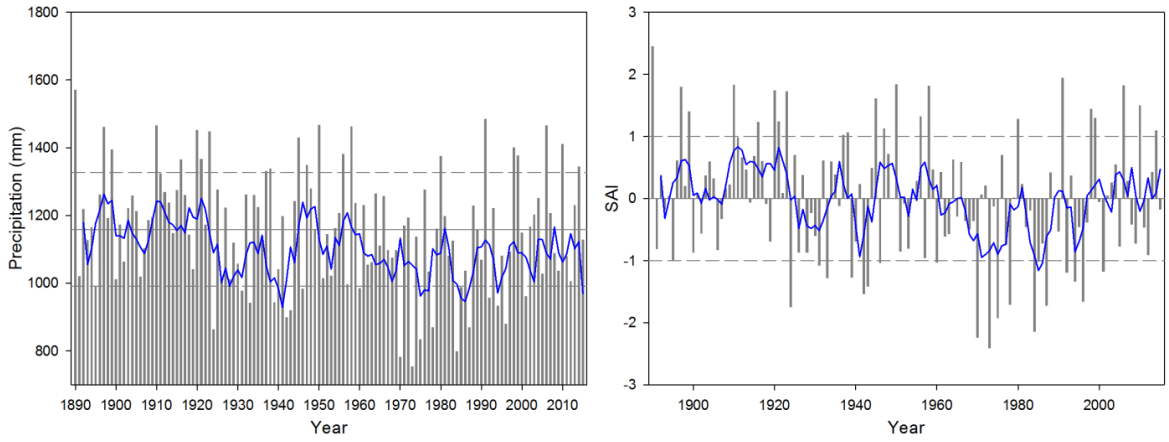

Figure 4. Mean annual precipitation (A) and the standardized anomoly index (SAI - B) for three long-term rainfall stations including mean annual precipitation (solid line), the standard deviation (dashed line) for the entire period and with the 5-year running average (blue line).

735

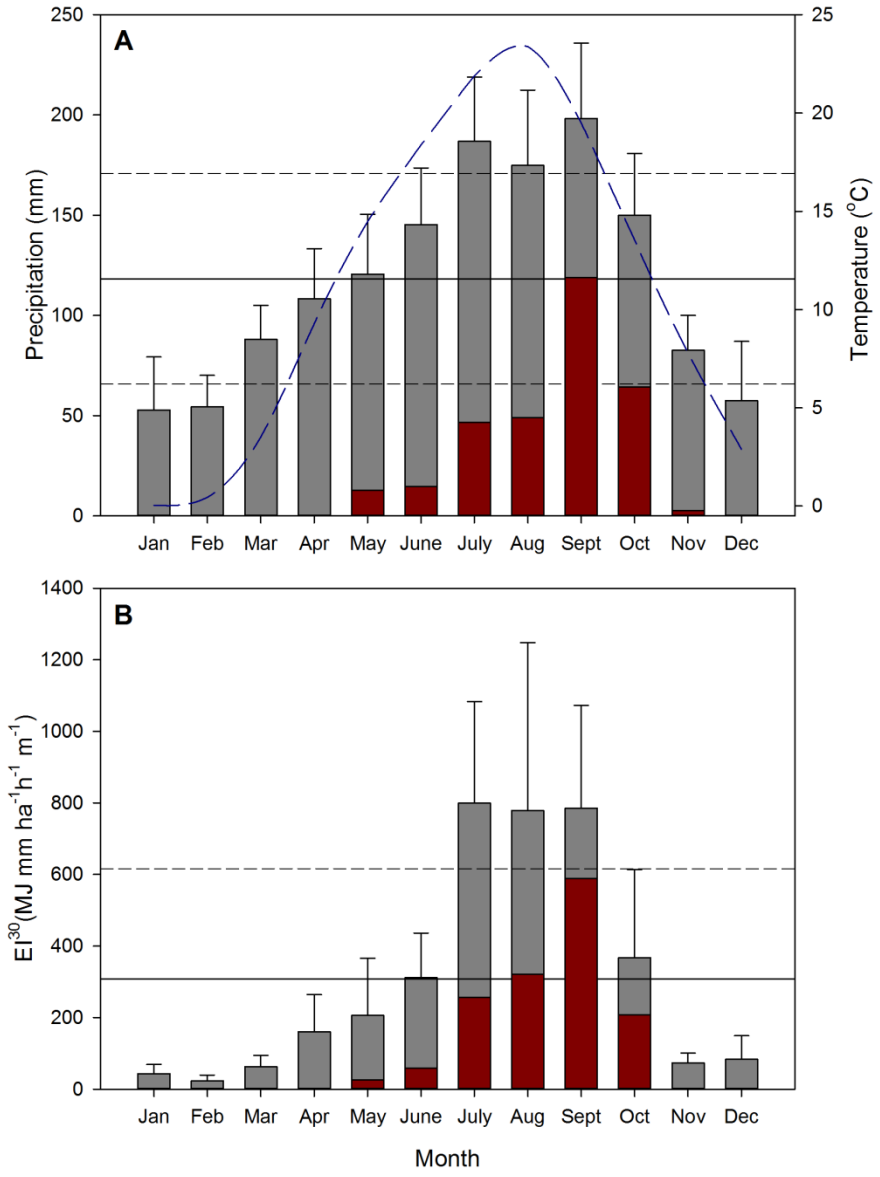

Figure 5. Total (grey) and typhoon related (red) mean monthly rainfall (A-top) and R-factor (B-bottom) with error bars indicating one standard deviation on the mean and the solid line representing the monthly mean and dashed lines representing on standard deviation on the mean. The mean monthly temperature is plotted (red line) along with mean monthly rainfall (A-top).

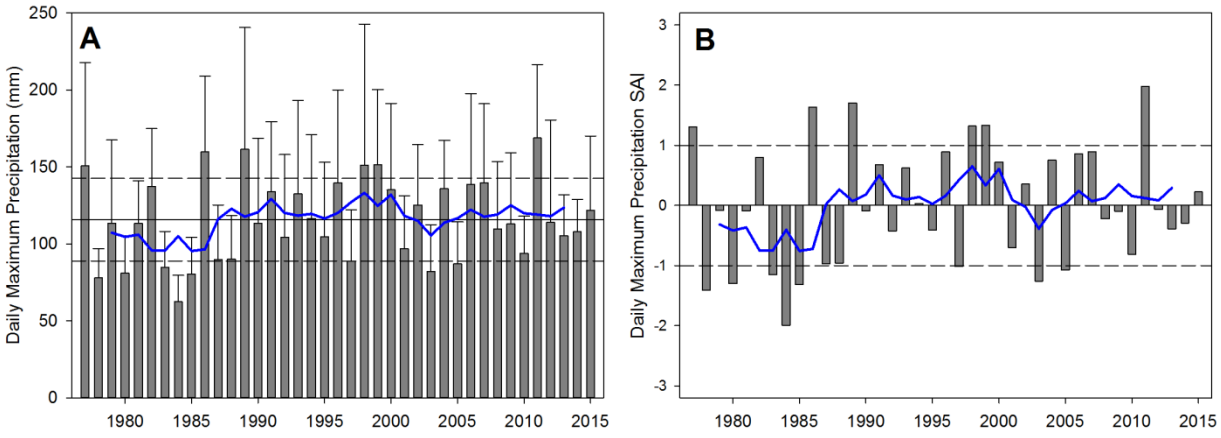

Figure 6. Mean maximum daily precipitation (A) and corresponding SAI with error bars indicating one standard deviation on the mean for each station, along with the mean (solid) and one standard deviation on the mean (dashed line) for the daily rainfall analyses period and the blue solid line depicting the 5-year running average.

736

737

738

739

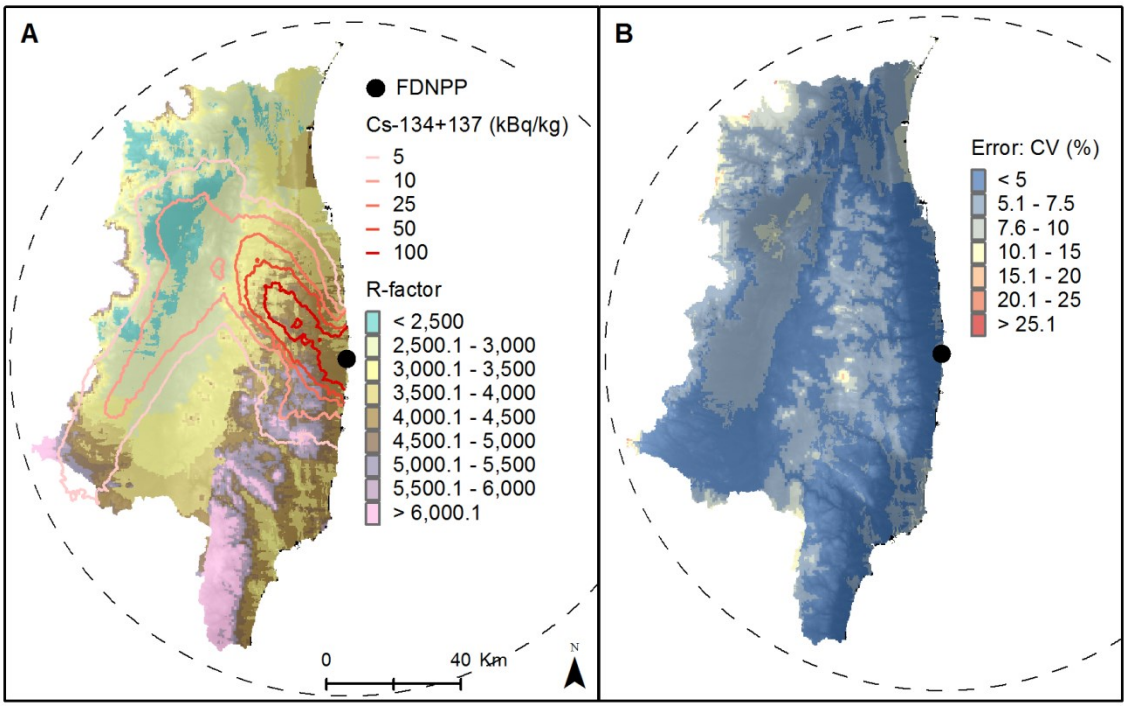

740

741 **Figure 7:** Annual R-factor (A) and model errors depicted as the coefficient of variation (i.e. CV=
742 (standard error / mean) *100) (B) for catchments entirely contained within a 100 km radius of the
743 FDNPP. $^{134+137}$Cs activities are from Chartin et al. (2013).

744

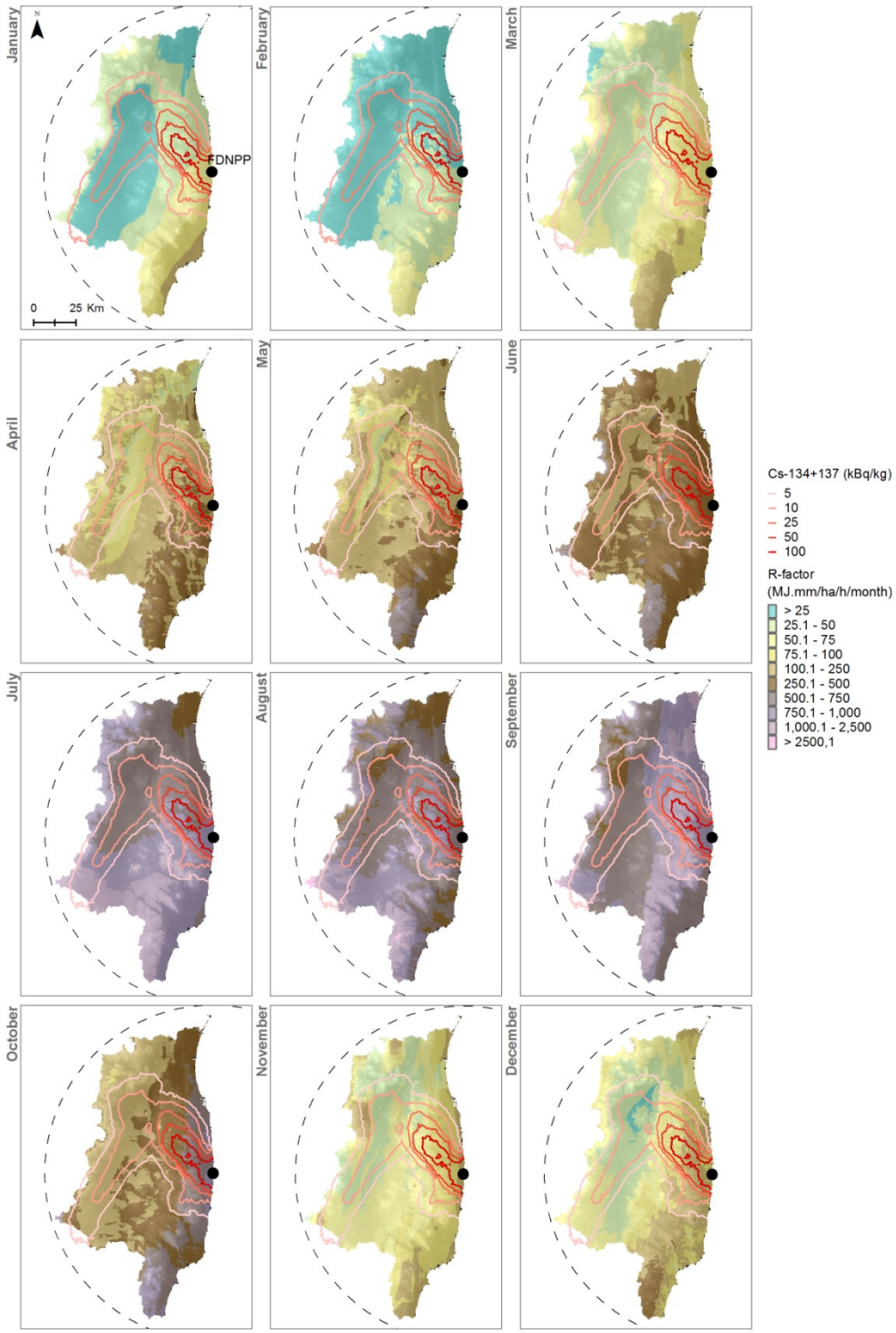

745

746 **Figure 8.** Monthly R-factor distribution for catchments contained entirely within a 100 km radius
747 of the FDNPP. $^{134+137}$Cs activities are from Chartin et al. (2013).

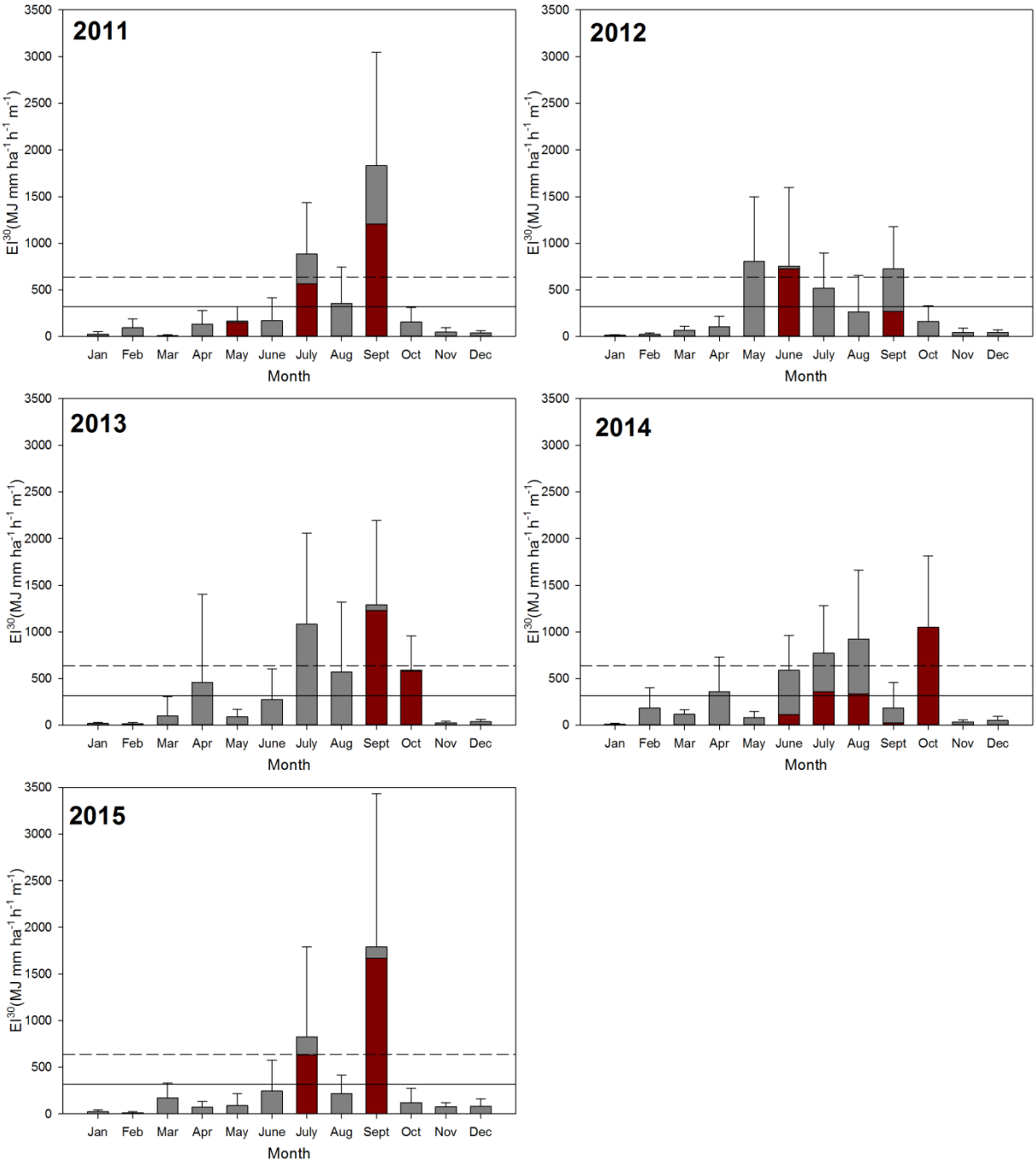

Figure 9. Total (grey) and typhoon related (red) monthly rainfall erosivity from 2011–2015 with the mean line representing mean monthly rainfall erosivity and the dashed line being one standard deviation on the mean for the period of 1995-2015 for the 42 rainfall stations analyzed.

748